Pump–probe experiments at the TEMPO beamline using the low-α operation mode of Synchrotron SOLEIL

Mathieu G Silly, Tom Ferté, Marie Agnès Tordeux, Debora Pierucci, Nathan Beaulieu, Christian Chauvet, Federico Pressacco, Fausto Sirotti, Horia Popescu, Victor Lopez-Flores, et al.

JOURNAL OF SYNCHROTRON RADIATION
ISSN 1600-5775

Received 8 March 2017
Accepted 28 May 2017

Edited by I. Schlichting, Max Planck Institute for Medical Research, Germany

‡ Present address: Centro Atómico Constituyentes CNEA and Concejo Nacional de Investigaciones científicas y técnicas, Buenos Aires, Argentina.
§ Present address: Department of Physics, Jadavpur University, Kolkata 700032, India.

Keywords: time-resolved spectroscopy; pump–probe experiments.

Pump–probe experiments at the TEMPO beamline using the low-α operation mode of Synchrotron SOLEIL

Mathieu G. Silly,[a] Tom Ferté,[b] Marie Agnes Tordeux,[a] Debora Pierucci,[a,c] Nathan Beaulieu,[a] Christian Chauvet,[a] Federico Pressacco,[a] Fausto Sirotti,[a,d]* Horia Popescu,[a] Victor Lopez-Flores,[a] Marina Tortarolo,[a]‡ Maurizio Sacchi,[a,e] Nicolas Jaouen,[a] Philippe Hollander,[a] Jean Paul Ricaud,[a] Nicolas Bergeard,[b] Christine Boeglin,[b] Bharati Tudu,[c]§ Renaud Delaunay,[c] Jan Luning,[c,a] Gregory Malinowski,[f] Michel Hehn,[f] Cédric Baumier,[g] Franck Fortuna,[g] Damjan Krizmancic,[h] Luigi Stebel,[i] Rudi Sergo[i] and Giuseppe Cautero[i]

[a]Synchrotron SOLEIL, L'Orme des Merisiers, Saint Aubin, Gif sur Yvette 91192, France, [b]Université de Strasbourg, CNRS, Institut de Physique et Chimie des Matériaux de Strasbourg, UMR 7504, F-67000 Strasbourg, France, [c]Sorbonne Universités, UPMC Université Paris VI, CNRS, Laboratoire de Chimie Physique – Matière et Rayonnement, Paris 75005, France, [d]Laboratoire de Physique de la Matiére Condensée, UMR 7643, CNRS and Ecole Polytechnique, Université Paris Saclay, Palaiseau 91128, France, [e]Institut des NanoSciences de Paris, Sorbonne Universités, UPMC, CNRS, UMR 7588, Paris 75005, France, [f]P2M – Institut Jean Lamour UMR7198, CNRS – Université de Lorraine, Vandoeuvre-les-Nancy 54506, France, [g]CSNSM, Université Paris Sud and CNRS/IN2P3, Batiment 104 et 108, Orsay 91405, France, [h]Laboratorio TASC, IOM-CNR, SS 14 Km 163.5, Basovizza, I-34149 Trieste, Italy, and [i]ELETTRA Sincrotrone Trieste SCpA, Area Science Park, Strada Statale 14 Km 163.5, I-34012 Basovizza, Italy.
*Correspondence e-mail: fausto.sirotti@synchrotron-soleil.fr

The SOLEIL synchrotron radiation source is regularly operated in special filling modes dedicated to pump–probe experiments. Among others, the low-α mode operation is characterized by shorter pulse duration and represents the natural bridge between 50 ps synchrotron pulses and femtosecond experiments. Here, the capabilities in low-α mode of the experimental set-ups developed at the TEMPO beamline to perform pump–probe experiments with soft X-rays based on photoelectron or photon detection are presented. A 282 kHz repetition-rate femtosecond laser is synchronized with the synchrotron radiation time structure to induce fast electronic and/or magnetic excitations. Detection is performed using a two-dimensional space resolution plus time resolution detector based on microchannel plates equipped with a delay line. Results of time-resolved photoelectron spectroscopy, circular dichroism and magnetic scattering experiments are reported, and their respective advantages and limitations in the framework of high-time-resolution pump–probe experiments compared and discussed.

1. Introduction

Synchrotron-radiation-based spectroscopy techniques have encountered enormous success over the last 30 years. The interaction of radiation with matter has become a powerful tool in all scientific domains, from physics to chemistry, from geology to biology (Funk *et al.*, 2005). Theoretical approaches have been developed to explain and predict many details observed in spectroscopic signals. All these developments are based on the assumption that absorption or diffusion of a single X-ray photon is characterized by small amounts of energy with respect to that of the system to be studied. The high repetition rate of synchrotrons with a small number of photons per pulse is well adapted to the description of the single-photon/matter interaction.

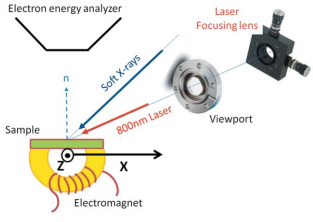

First time-resolved experiments using soft X-ray synchrotron radiation were based on partial filling of the storage ring (Sirotti *et al.*, 2000; Bonfim *et al.*, 2001) to obtain a small reduction of repetition rate and cope with excitation repetition rate and decay times. Time resolution, limited mainly by the synchrotron radiation pulse duration, has been improved at third-generation sources, where the limit in normal operation is 50 ps FWHM (Couprie & Filhol, 2008).

Recently developed free-electron lasers (FELs), plasma (Bargheer *et al.*, 2004) and high-harmonic generation (HHG) (Pfeifer *et al.*, 2006) sources are capable of producing short pulses over the whole wavelength range from ultraviolet radiation to hard X-rays with pulse durations that clearly outperform synchrotron radiation sources. The characteristics of FEL X-ray beams amaze because of the number of photons per pulse resulting in extremely high photon density. They have opened the way to new kinds of experiments instead of performing synchrotron radiation techniques more effectively: one shot is sufficient to extract all the information needed to characterize the studied system. The Flash FEL in Hamburg demonstrated 6×10^3 X-ray pulses per second (Ayvazyan *et al.*, 2006) and has further increased the number since then (Faatz *et al.*, 2011). These pulses of a few tens of femtoseconds in duration come as bunch trains at 10 Hz repetition rate. The FERMI FEL in Trieste is characterized by variable-polarization soft X-ray pulses with 100 fs durations and repetition rates up to 50 Hz (Allaria *et al.*, 2012). They cover a large energy range from the UV to the soft X-ray range with intensities of $\sim 10^{12}$ photons pulse^{-1}, largely exceeding the damage threshold for ordinary solid samples.

FELs capable of delivering short pulses of hard X-ray photons are best suited for time-resolved experiments considering magnetic and structural dynamics in solids and molecules. The Linac Coherent Light Source (LCLS) has demonstrated FEL operations over the 280 eV to 11.2 keV energy range. Third-harmonic radiation is available up to 25 keV at about 1% of the fundamental pulse intensity. The pulse length can be varied from 40 fs to 300 fs for hard X-rays, while for soft X-rays the range is extended to 500 fs. Shorter pulses (<10 fs) with a reduced number of photons per pulse can also be provided. The maximum repetition rate at LCLS is 120 Hz. The European X-ray Free Electron Laser (XFEL) in Hamburg plans to deliver photons between 200 eV and 12.4 keV with pulse durations of 100 fs at 27 kHz repetition rate. SACLA, the Japanese FEL facility, is now the only XFEL operating below 1 Å wavelength. The photon energy range can reach more than 20 keV with pulse durations as short as 2 fs. The repetition rate is 60 Hz (Yabashi *et al.*, 2015). Recently SACLA also opened a soft X-ray beamline (SXFEL).

The peculiar characteristics of XFEL sources allow users to imagine new experimental approaches in material science and, in particular, to address new states of matter. These large-scale facilities work mostly in single-experiment mode, which limits considerably their access to the user community. Moreover, because of the large number of photons per pulse and of the low repetition rate, performing standard spectroscopy experiments is usually complex at these installations (Higley *et al.*, 2016).

The fast development of laser sources is creating new effective possibilities for femtosecond and attosecond time-resolved experiments. Novel table-top sources of extreme-ultraviolet light based on HHG in gases yield unique insight into the fundamental properties of molecules, nanomaterials and correlated solids, enabling advanced applications in imaging and metrology. Bright high-repetition-rate sources of narrowband extreme-ultraviolet harmonics beyond 22 eV can now be obtained with repetition rates of 50 kHz (Wang *et al.*, 2015; Buss *et al.*, 2016). Photon energies in excess of 100 eV can be obtained with kHz sources suitable for photoelectron spectroscopy experiments (Ojeda *et al.*, 2016). Circular dichroism experiments at the *N*-edges of rare-earths have been performed with circularly polarized HHG sources (Fan *et al.*, 2015). Kilohertz sources can reach 0.5 keV photon energy, opening the way to the realisation of X-ray absorption spectra of the C *K*-edge and light transition metals with sub-femtosecond time pulses (Silva *et al.*, 2015; Teichmann *et al.*, 2016). The given references point to only a few of the results from the expanding scientific community using HHG short-pulse sources.

The specificity of the above-mentioned sources leads to the conclusion that synchrotron radiation sources remain essential and indispensable for high-quality spectroscopic research. The development of specific beamlines and optimized instrumentation matching each source characteristics and open to a wide user community are the strengths of synchrotron sources. At these sources, the high repetition rate, the extremely wide photon energy range and the user-controlled energy and polarization tunability are of prime importance. Although time resolution is limited to the picosecond range, these characteristics make synchrotron radiation an essential tool in every field of research, including material science developments. Many fundamental open questions and technological targets implying dynamics can be addressed with the time resolution available at synchrotrons.

Worldwide, machine physics groups are working on shortening the pulse length at synchrotron sources, for example using the slicing mode (Schönlein *et al.*, 2000; Stamm *et al.*, 2007; Ingold *et al.*, 2007; Boeglin *et al.*, 2010; Radu *et al.*, 2011; Wietstruk *et al.*, 2011; Prigent *et al.*, 2012; Lopes-Flores *et al.*, 2012, 2013; Bergeard *et al.*, 2014). A few hundred femtosecond pulse duration can be obtained with a few kHz repetition rate by using the electric field of an infrared (IR) laser to slice the electron bunches.

An alternative solution to reduce the pulse length at synchrotrons is to work on the electron optics by using low-momentum compaction factor operation (low-α mode) (Abo-Bakr *et al.*, 2003; Khan *et al.*, 2006; Kozina *et al.*, 2014; Tordeux *et al.*, 2012). In this work we describe the performance of the SOLEIL operation in low-α mode and the installations dedicated to pump–probe experiments with soft X-rays. We describe examples of applications in core-level photoemission, resonant core-level photoemission with circular-polarized X-rays and resonant magnetic scattering. Spectroscopic

Table 1
Parameters of different storage-ring operations *versus* momentum compaction factor, in terms of RF voltage, bunch length and bunch current.

		Camshaft bunch		Bunches in the train		
α value	RF voltage (MV)	Length (ps) FWHM	Current / charge (μA) / (pC)	Number of bunches	Length (ps) FWHM	Current / charge (μA) / (pC)
$\alpha/1$	2.7	62	5000 / 5900	312	48.4	1400 / 1650
$\alpha/25$	3.2	11	65 / 77	200 or 300	13	95 / 112
$\alpha/100$	4	7	15 / 18	200 or 300	7	15 / 18

performance is based on endstations and beamlines characteristics, but the final results are strongly dependent on the short laser pulse installation, on the synchronization system and on the detection systems used for photon and electron counting. The aim is to identify the limits imposed by the reduced photon flux and by the specific time structure on well mastered techniques currently used to describe the electronic structure and the magnetic order of materials.

2. Low-α mode at SOLEIL

As with many synchrotron light sources, the optics of SOLEIL's storage ring is optimized for high brilliance at high flux with bunch lengths exceeding 50 ps FWHM in the bunch train at 500 mA, as well as in the isolated (camshaft) bunch in hybrid mode at 450 mA. One way to reduce this length consists of changing the ring optics to render it more isochronous. The relevant figure of merit is then the relative change of the circumference of a particle orbit around the storage ring as a function of the momentum deviation of the particle: $\Delta L/L_0 = \alpha\,\Delta P/P_0$. α is the momentum compaction factor of the optics and $\Delta P/P_0$ is the relative momentum deviation of the particle compared with the synchronous one. As optics dedicated to pump–probe experiments exhibit an α value reduced by a factor of 25–100 compared with the nominal optics, this mode is called low-α.

The measured low-α bunch length reduction is shown in Fig. 1 for different values of α and of the radio-frequency (RF) cavities voltage. The resulting total stored current, as well as the hybrid filling pattern of the low-α operations, are summarized in the inset of Fig. 1. More detailed values of bunch length and bunch current are listed in Table 1. $\alpha/10$ is indicated by red symbols, $\alpha/45$ by blue symbols and the $\alpha/1$ standard operation is the black circle. The pulse duration scales as the square root of α, for a very low current per bunch. Moreover, due to collective effects, an important elongation of the bunch is observed and enhanced with the current. This is the main reason to strictly limit the current per bunch to a few tens of μA (*i.e.* the bunch charge to a few tens of pC). Following these limitations, bunch lengths for user operation have been obtained with 11 ps FWHM [7 ps FWHM] in the $\alpha/25$ mode [$\alpha/100$ mode] for the camshaft bunch. The spacing between bunches (2.8 ns) and the maximum repetition rate (352 MHz) remain the same as in the standard operation mode. Comparable pulse duration and currents per bunch are obtained at BESSY II (Jankowiak & Wüstefeld, 2013) and other facilities.

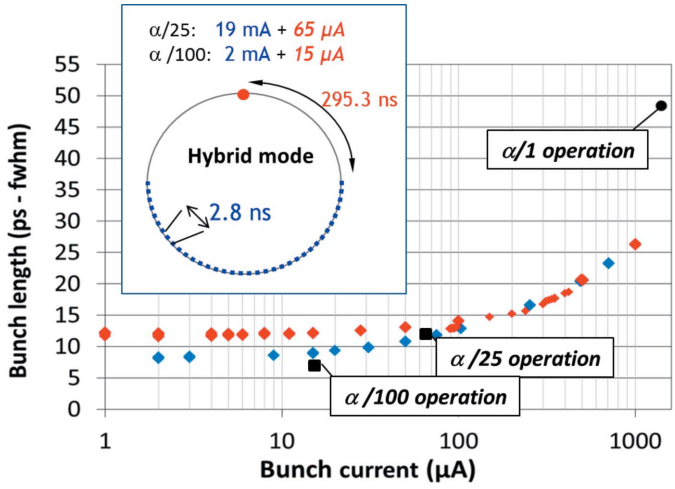

Figure 1
Electron bunch lengthening with current in low-α mode, for different values of the momentum compaction factor α. Operation characteristics of the isolated bunch are shown by square points. Inset: filling pattern and total stored current for the low-α operations.

An important issue is the increased sensitivity to energy oscillations that are transferred to the horizontal plane with a factor of 25 or 100 compared with the nominal operation. At SOLEIL, thanks to a solid-state-based RF system on the one hand, and to an efficient fast orbit feedback system, on the other hand, an excellent stability in both longitudinal and transverse planes is preserved. Fig. 2 shows how the degradation from the normal operation has been contained.

The average Fourier transform amplitude measured as a function of the frequency by the SOLEIL electron beam position monitors is presented in the top panel for the horizontal and vertical planes. The results for $\alpha/25$ (in red) are compared with the same measurements performed in normal operation ($\alpha/1$). The noise measured as a function of the frequency for the two operation modes is compared in the bottom panel of Fig. 2. It remains below 1 μm in the horizontal plane and 0.34 μm in the vertical, guaranteeing the same photon beam characteristics of the normal operation conditions after energy selection and focusing mirrors as the TEMPO beamline.

3. Soft X-rays and laser system installations

Synchrotron radiation emitted by two APPLE II insertion devices with 44 mm and 80 mm periods is monochromated and

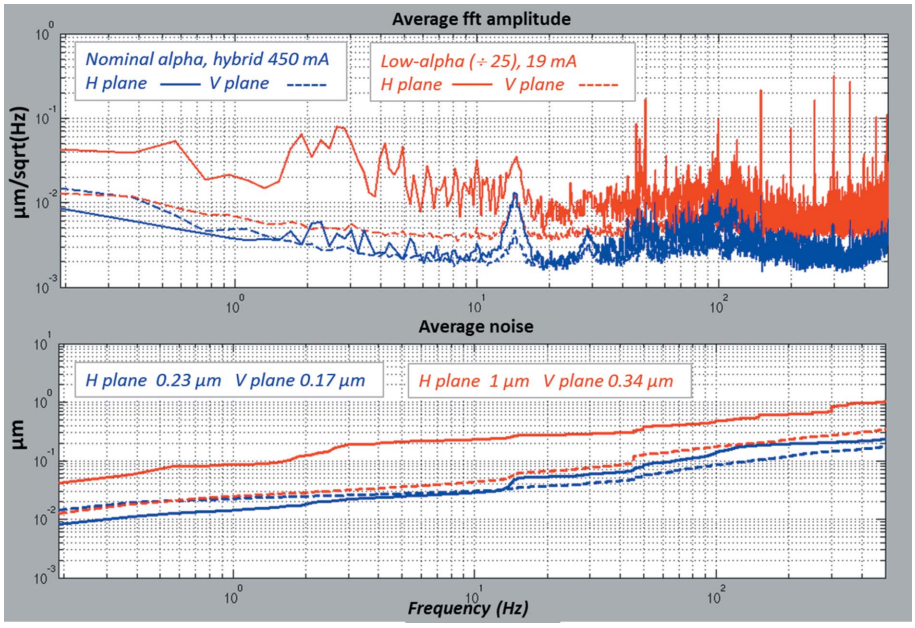

Figure 2
Power spectral density (top) and integrated noise (bottom) until 500 Hz in the presence of the fast orbit feedback system, for nominal-α optics (α = 4.2 × 10–5) and low-α optics ($\alpha = 1.7 \times 10^{-5}$).

transported to two experimental stations (Polack *et al.*, 2010). The photon energy ranges between 50 and 1500 eV. In terms of flux and energy resolution and focusing, the insertion devices and beamline characteristics are not modified by the low-α operation. The photon flux scales with the bunch current values reported in Table 1, with about 1×10^7 photons s^{-1} μA^{-1} in the bunch used for pump–probe experiments. This corresponds to about 100 photons $pulse^{-1}$ in $\alpha/100$ operation. Note that about the same number of photons per pulse will be obtained in future femto-slicing experiments but at a lower repetition rate. Two experimental stations were used for low-α experiments. The UHV photoemission station installed on the direct branch was used for surface photovoltage experiments on SiO_2/Si interfaces and laser-induced surface demagnetization experiments on CoGd layers. The SEXTANTS beamline experimental station for coherent imaging (Sacchi *et al.*, 2013) installed on the second branch line was used to measure fast demagnetization processes in CoPd layers on membranes. The soft X-ray spot size was measured using a YAG crystal and has a FWHM smaller than 100 µm at the two branches in order to be adapted to the laser focal spots. Details are given in §4.

Sudden modifications in physical and chemical properties can be induced by a femtosecond pulsed laser. Although the probe resolution is limited to the picosecond regime, it is important to control the pump length for significant experiments, since pulse duration, and hence peak power, can strongly influence the system response to the excitation. Magnetization dynamics (Beaurepaire *et al.*, 1996), catalytic reactions at surfaces (Bonn *et al.*, 1999) and, in general, specific final states can be influenced by distributing the same total pulse energy over different time scales. The average deposited energy can be the same but the physics induced by femtosecond laser excitations can be extremely different.

The laser system (REGA Coherent) was chosen in order to produce femtosecond laser pulses with the highest possible repetition rate but with enough energy per pulse to obtain a fluence of a few mJ cm^{-2} at the sample position. Specific electronics were developed by Coherent to produce laser pulses synchronized with SOLEIL synchrotron radiation (Synchrolock, Coherent). The maximum available frequency is 282 kHz which corresponds to three SOLEIL revolution periods. The Coherent REGA femtosecond laser is installed in a dedicated hutch at the TEMPO beamline. A dedicated laser beamline was installed to bring the class IV laser radiation to the UHV experimental stations at about 15 m downstream. In order to fulfil safety requirements, the transport line is hermetically sealed and the UHV experimental chambers are equipped with metallic protections on all viewports. A double key safety system prevents the user from being exposed to the laser beam. A lens with a focal distance of 500 mm is the last optical element before entering the experimental station viewport. By adjusting the longitudinal lens position, the laser focal spot can be reduced to a minimum diameter of 210 µm.

4. Spatial alignment of synchrotron and laser beams

Stable and reliable spatial alignment of synchrotron and laser beams is an essential point for pump–probe experiments. We have evaluated the energy density per pulse necessary to induce phase transitions and fast demagnetization processes at 4 mJ cm^{-2}. Operating at high repetition rates imposes focusing the laser beam to a diameter of few hundreds of micrometres. Owing to soft X-ray focal distances and UHV constraints, two different approaches were adopted in the two beamline branches. A schematic view of the experimental setup is presented in Figs. 3(*a*) and 3(*b*). In the UHV photoemission experimental station the surface normal is usually oriented along the electron energy analyser axis and the soft X-ray beam impinges on the surface at 43° from the surface normal. The laser beam is about 24° grazing incidence. The X-ray focal spot was measured on a YAG fluorescent crystal placed at the sample position, using a CCD camera. The laser focal spot is observed by the same camera on a gold clean surface. The measured images are presented in Figs. 4(*a*) and 4(*b*). The absolute values on the horizontal (X) and vertical (Z) axis are obtained by scanning a 25 µm photodiode around the sample position in the presence of the laser beam. The beam profiles in the two directions are presented in Figs. 4(*c*) and 4(*d*) for the horizontal and vertical directions, respec-

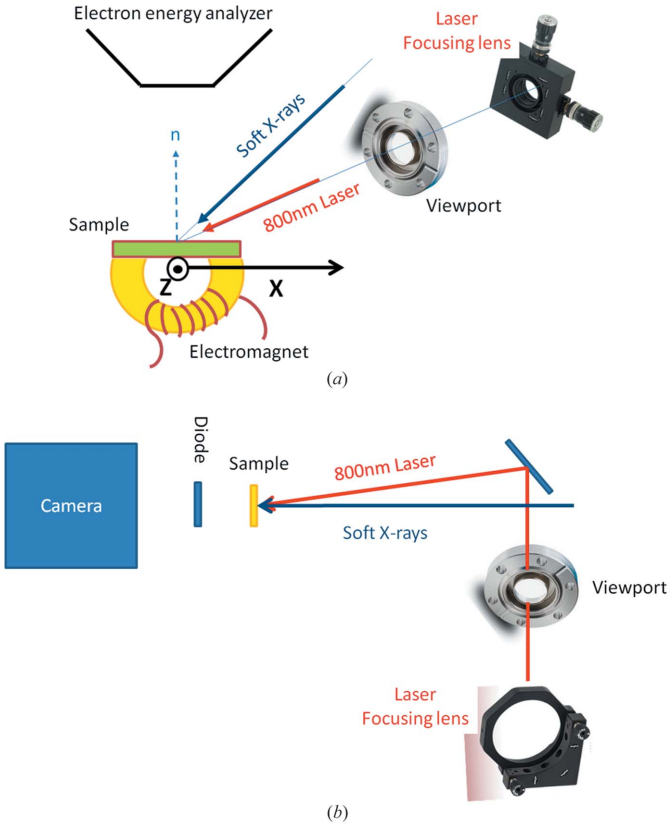

Figure 3
Schematic view of the experimental setup in the UHV photoemission (*a*) and in the X-ray scattering (*b*) experimental stations.

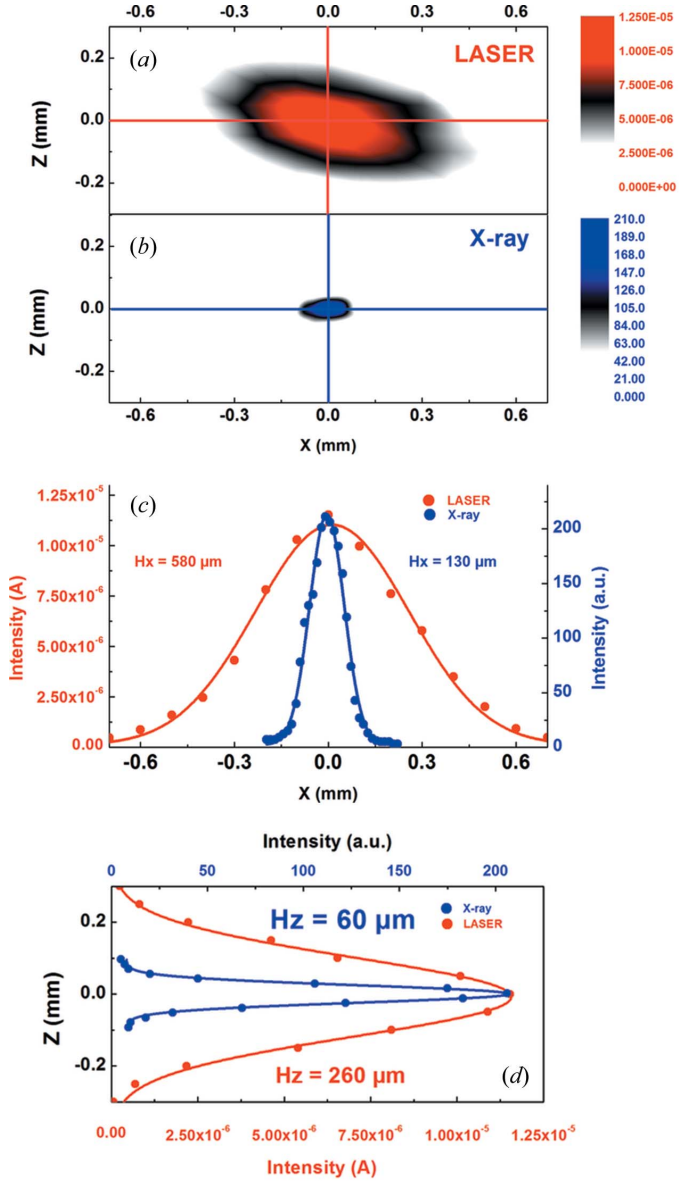

Figure 4
Spatial alignment of synchrotron and laser beams in the UHV photoemission experimental station. Panels (*a*) and (*b*) show the focal spots of laser and X-rays, respectively, as measured at the sample position by a CCD camera. X-rays are imaged on a YAG crystal and laser photons on a gold single-crystal surface. Beam profiles on the two orthogonal axis are reported in panels (*c*) and (*d*).

tively. Gaussian fits give the horizontal and vertical focal spots indicated in Fig. 4.

The same experiment performed with soft X-rays allows us to image the diode metallic contacts and wiring. This is sufficient to place the synchrotron beam at the centre of the diode. A focusing lens placed before the UHV chamber entrance is then used to displace the laser beam in order to maximize the diode signal and optimize the spatial overlap of the two photon beams.

A schematic view of the scattering experimental station installed at the branch line is presented in Fig. 3(*b*): a mirror is placed at 45° near the X-ray beam axis at 300 mm from the sample. The laser focusing lens with a focal distance of 500 mm is placed in air. Experiments were performed on CoPd multilayers deposited on X-ray transparent SiN membranes, with both synchrotron and laser beams impinging at normal incidence. A diode placed behind the membrane was used for spatial alignment. The highest laser power density was used to burn one membrane onto a 50 µm surface. The hole was aligned on the soft X-ray beam and then the laser was aligned through the hole for spatial superposition. The laser was focused to about 80 µm FWHM, which allowed us to achieve a pump fluence of 20 mJ cm^{-2}. Since the X-ray probe pulse (∼100 µm FWHM) is larger than the IR pump pulse, a 50 µm pinhole was placed before the sample to ensure that the X-rays are probing a uniformly excited area.

5. Synchronization

The laser oscillator frequency is controlled by the SOLEIL RF signal divided by four (88 MHz). The regenerative amplifier stage of the laser and the experimental setups are triggered with TimBeL boards. They allow the users to adjust delays with a resolution of about 20 ps and trigger frequencies from 88 MHz down to 44 MHz (Ricaud *et al.*, 2011). One channel is used to extract selected laser pulses from the REGA amplifier at selectable frequencies synchronized with the SOLEIL RF. A synchronization electronics schematic diagram during a phase noise jitter measurement is presented in Fig. 5. The IQ modulator is used to change the phase of the laser oscillator

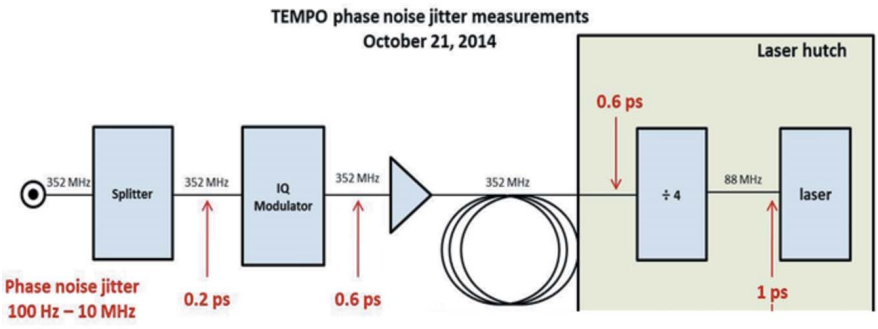

Figure 5
Laser/synchrotron synchronization system during a phase noise jitter measurement in the frequency range between 10 Hz and 10 MHz. The output of the IQ modulator is amplified, transported to the laser hutch and divided by four. It is the reference signal for the Coherent Synchronization system.

and fine-tune the delay between synchrotron radiation and laser pulses. It is controlled with two digital-to-analog converters and allows the offset between the laser and the synchrotron pulses to be adjusted with a resolution of ± 2.5 ps after correction and a phase noise jitter of 1 ps (100 Hz to 10 Mhz; @88 MHz). Phase noise measurements performed to characterize the total error introduced confirmed a noise jitter below 1 ps.

6. Two-dimensional time-resolved detection

The SOLEIL time structure presented in the inset of Fig. 1 deserves a more detailed description taking into account the spectroscopic applications. Only the isolated bunch is used for pump–probe time-resolved photoemission spectroscopy, since the spread of electron trajectories in the electron energy analyser imposes at least 100 ns separation between the photoelectrons carrying the information on the laser excitation and those generated by other synchrotron pulses. The signal from other electron bunches is well separated from that of the isolated one. Their photon flux is precious for performing spatial alignment procedures and characterizing samples before pump–probe experiments. In photon scattering experiments the detector can easily identify single-bunch emission also in the bunch sequence with 2.8 ns separation. For these experiments it is then more convenient to perform pump–probe measurements by scanning the laser delay only between two synchrotron pulses separated by 2.8 ns in order to obtain ultimate time-resolution spectra in a wide time interval. Both photons and photoelectrons are measured with space and time resolution by using a delay line detection scheme (Cautero *et al.*, 2008) that collects the electron cloud generated at each single event by a stack of micro-channel plates. Two different two-dimensional space resolution plus time resolution (2D+t) detectors and electronics were optimized for electron and photon detection. In the photon detection scheme, the spatial resolution of the detector is used to measure the angular distribution of scattered photons. In the electron detection experiment, the 2D+t detector is installed after a Scienta SES 2002 hemispherical electron energy analyzer and the two directions in space resolve the kinetic energy and emission angle of the photoelectrons.

For photon counting, fast electronics allow us to push time resolution to a few hundreds of picoseconds. The time structure of SOLEIL's hybrid filling pattern obtained by measuring photons is presented in Fig. 6. It is easy to recognize the isolated bunch and the three-quarters of the ring filled with 300 bunches spaced with 2.8 ns period. The zoom reported in the inset reveals the X-ray flashes of the individual electron bunches and characterizes the time resolution of the detection scheme.

When photoelectrons are measured, the arrival time at the detector is influenced by the electron trajectories within the analyser which give rise to a much longer time spread. The electronics have been adapted to a simpler signal handling related to the operation with the electron energy analyzer software and it allows a time resolution of 5 ns to be obtained (Bergeard *et al.*, 2011).

7. Software

Dedicated *Labview* software was developed for time-resolved data acquisition. Measured events are treated in real time during the acquisition process in order to reconstruct scattering images and photoemission spectra as a function of time. With respect to the direct storage of each independent event this procedure strongly reduces memory needs. The partially treated data can also be used to follow the measurement progress in real time and to verify spatial and time alignment. An example of the acquisition window in photoemission experiments when measuring a thin SiO_2 layer grown on Si(100) is shown in Fig. 7. Spectra measured with eight revolutions of electrons in the storage ring are presented in the top

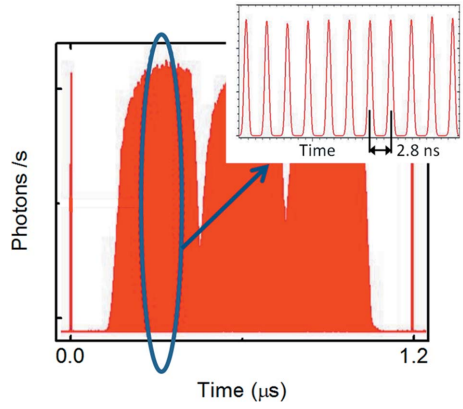

Figure 6
Intensity of the X-ray pulses emitted by the electron bunches of SOLEIL's hybrid mode fill pattern as measured with the time-resolved delay line photon detector. The isolated bunch is at $t = 0$ and $t = 1.2$ μs. The inset shows a zoom of the bunch sequence with the light pulses separated by 2.8 ns.

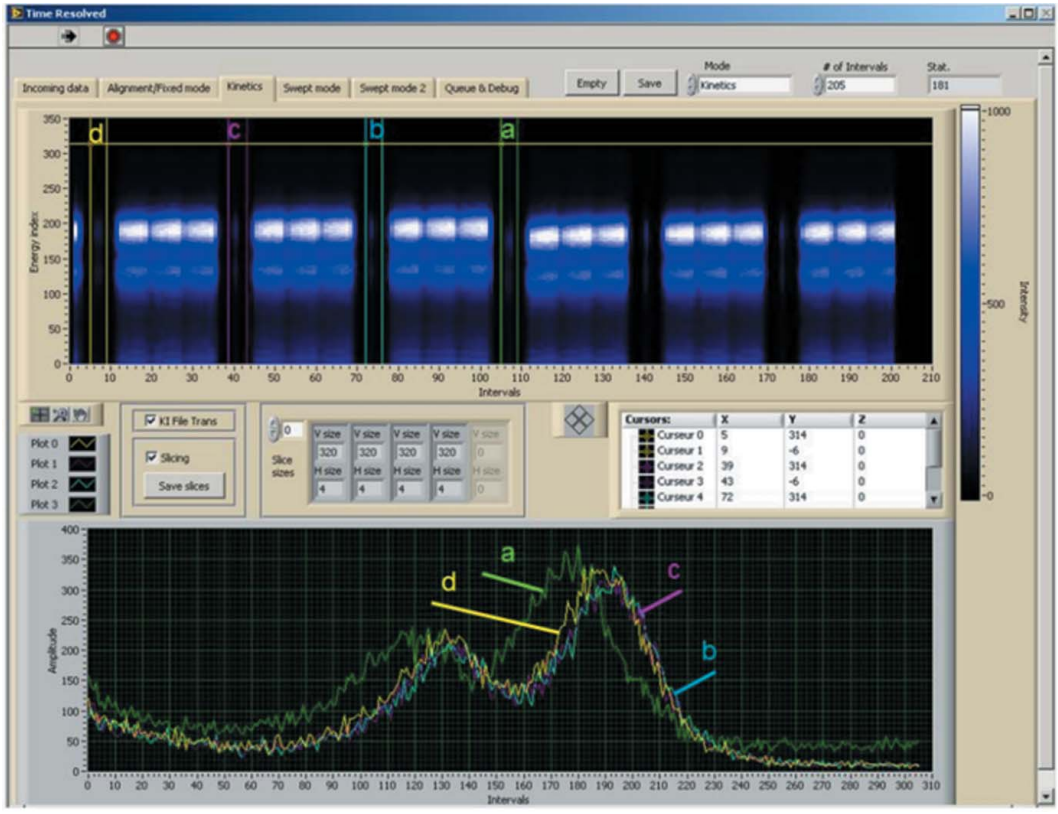

Figure 7
Example of the acquisition window of the time-resolved acquisition software when measuring a thin SiO_2 layer grown on Si(100). In the top panel the photoemission intensity distribution is presented on a colour scale as a function of kinetic energy (vertical axis) and time (horizontal axis). The bottom panel shows the Si-2*p* photoemission spectra integrated on the time intervals containing the signal from isolated synchrotron bunches. The cursors in the upper panel and the corresponding Si-2*p* curves in the lower panel have the same colour.

panel where photoelectron intensity is presented as a function of time channels on the horizontal axis and kinetic energy on the vertical one. The laser is synchronized just before the fourth revolution of the isolated bunch. We can follow in real time the modification of a photoemission peak during the laser excitation selecting the fourth passage of the bunch synchronized with the laser pulse (an interval within the green cursors), the green curve in the bottom panel of Fig. 7, and to make a comparison with the signals coming from the other isolated synchrotron bunches for which the delays from the laser excitation are larger (*b*, *c* and *d* and corresponding colours).

8. Applications

The presented installations are well suited for photoelectron spectroscopy and scattering pump–probe experiments at a selectable repetition rate defined by the REGA laser settings. The higher the laser repetition rate, the higher the number of synchrotron pulses available to measure the laser-induced excited state, providing better statistics. At the expense of count rate, the repetition rate of the excitation can be reduced to deal with longer relaxation times of the phenomena to be observed. In the following we give three examples of possible applications, namely surface photovoltage effects in SiO_2/silicon interfaces, surface magnetization dynamics measured by resonant Auger intensity in CoGd alloys and resonant magnetic scattering in CoPd layers.

8.1. Surface photovoltage

Surface/interface photovoltage effects are the modification of the charge equilibrium at a semiconductor interface following an electronic photoexcitation. They are important in defining the performance of an electronic device because they define the charge carrier's dynamics across the interface and are directly related to relevant quantities in semiconductor and solar cell technology. Time-resolved photoemission of core electron binding energies is a direct measurement of the surface photovoltage (SPV) potential and band bending lowering due to the absorption of visible photons. The time profile of the SPV effect can be directly obtained following the core-level energy shift under laser excitation. Several time-resolved core-level photoemission studies combining synchrotron radiation with pulsed laser sources (Long *et al.*, 1990; Widdra *et al.*, 2003; Ogawa *et al.*, 2013; Spencer *et al.*, 2013), including storage-ring FELs (Marsi *et al.*, 1997, 2000), have been performed to study the SPV effect on clean and oxidized silicon surfaces. To evaluate the potential of the technique in the SOLEIL low-α mode we have measured the

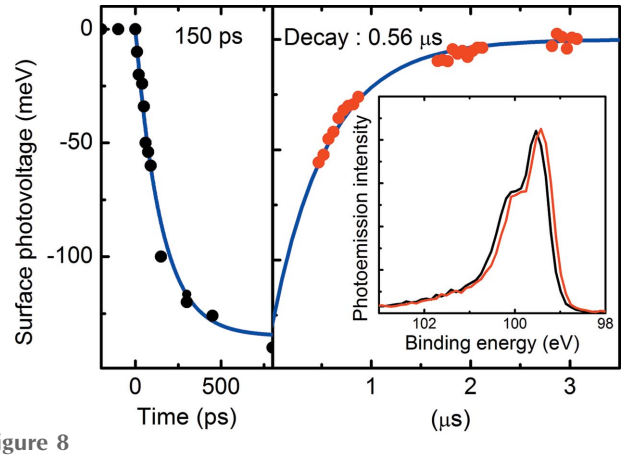

Figure 8
Left: kinetic energy shift measured as a function of the delay between the 50 fs laser excitation and the synchronized isolated synchrotron pulse in the α/25 SOLEIL filling mode. Right: kinetic energy shift measured during the decay process using the consecutive filling part of the synchrotron radiation time structure. The inset shows the Si-2*p* spectra measured before (black line) and 100 ps after (red curve) the laser excitation. Experiments were performed with 150 eV photon energy.

Si-2*p* core level at the interface between a thin SiO_2 layer grown on a Si(100)-2 × 1 surface after a 50 fs laser pulse excitation. The modification of the Si-2*p* core-level binding energy as a function of the delay between the laser pump and synchrotron radiation probe is shown in Fig. 8. Experiments were performed at a photon energy of 150 eV. The delay scale is separated into two regions with different increments to highlight the different time scales characterizing excitation and relaxation times. The blue line is the fitting curve obtained as the combination of two exponentials with coefficients of 150 ps for the growth and 560 ns for the decay. The inset compares Si-2*p* core-level spectra measured before (black curve) and 100 ps after (red curve) the 800 nm laser pulse excitation. The high cross section and the low background result in a good signal-to-noise ratio even for small count rates and makes it possible to detect small kinetic energy shifts. The whole experiment took 12 h with 30 min spent to measure each photoemission spectrum with a 10 ps delay step. Experiments were performed in α/25 mode.

8.2. Surface-sensitive X-ray magnetic circular dichroism (XMCD)

Surface-sensitive magnetization dynamics in the picosecond time scale is one of the scientific applications of the low-α operation mode at SOLEIL. The experiments were performed on CoGd alloys by measuring absorption at the Gd-M_5 resonance in Auger electron yield mode. The probing depth at this high-cross-section absorption edge is ∼15 Å (Vicentin *et al.*, 1995); therefore the $Co_{0.65}Gd_{0.35}$ film can be considered homogeneously pumped over the probed thickness. This kind of measurement is motivated by the wide range of characteristic demagnetization times reported in the literature for rare-earth systems. The reported demagnetization dynamics occur on two subsequent time scales ($\tau_1 \simeq 1$ ps and $\tau_2 \simeq 40$ ps) and the slower one is attributed to the strength of Gd-4*f* spin-lattice coupling (Wietstruk *et al.*, 2011). Recently, Frietsch *et al.* invoked the surface sensitivity of time-resolved ultraviolet photoelectron spectroscopy in single-crystalline Gd films (Frietsch *et al.*, 2015) to explain a different demagnetization time of ∼14 ps compared with the literature (Wietstruk *et al.*, 2011; Eschenlohr *et al.*, 2014; Rettig *et al.*, 2016). A different interpretation proposed by Koopmans *et al.* (2009) attributes the presence of two time scales to the Elliot–Yafet spin-flip mechanism. According to this model, the increase of the ordering temperature, as obtained in CoGd alloys for instance, should strongly modify the characteristic demagnetization times. Motivated by the prospective of testing the proposed models, we studied the laser-induced dynamics of the Gd-4*f* spins in a $Co_{0.65}Gd_{0.35}$ alloy, with the ∼11 ps time resolution of the low-α mode, by means of time-resolved photoelectron spectroscopy at the Auger Gd-M_5 resonance. The advantage of the spectroscopy is twofold. The surface sensitivity of the technique allows for a selective surface-dependent demagnetization dynamic of Gd-4*f* spins. Both XAS and XPS measurements performed at regular time intervals allow us to follow the chemical stability of the $Co_{0.65}Gd_{0.35}$ films.

The alloy was excited by IR femtosecond laser pulses at 800 nm while the transient magnetization was probed by using circularly polarized X-ray pulses tuned at the Gd-M_5 resonance. The fluence of the laser was 2 mJ cm^{-2} and the repetition rate was 141 kHz. These parameters were chosen as the best compromise between avoiding heating of the magnetic film and optimizing the photoemitted intensity. The M_5-VV Auger peak intensity was measured at the maximum of the M_5 absorption edge. This quantity is proportional to the X-ray absorption coefficient. Therefore the signal variation upon reversing the X-ray helicity or the external magnetic field is proportional to the gadolinium magnetic moment. Results are presented in Fig. 9 for the $Co_{0.65}Gd_{0.35}$ alloy. Auger signals measured before and 100 ps after the laser excitation are presented in panels (*a*) and (*b*). For positive delays (Fig. 9*b*) the XMCD is strongly reduced describing the laser-induced quenching of the magnetic order. The XMCD signal is integrated over the probed kinetic energy range and the difference (black circles) is shown as a function of the pump–probe delay in Fig. 9(*c*). The signal measured with the X-ray pulse synchronized with the laser excitation is normalized to the total signal generated by the other bunches of the hydride mode corresponding to the static magnetic state. The characteristic recovery time (not shown in the figure) measured in normal mode is 850 ps. The characteristic demagnetization time for the $Co_{0.65}Gd_{0.35}$ alloy extracted from the fit is 35 ± 10 ps. These preliminary pump–probe experiments demonstrate the potential of time-resolved XMCD based on the detection of Auger photoelectrons with 12 ps time-resolution to investigate the Gd-4*f* spin dynamics in pure rare-earth metals and alloys.

8.3. Magnetic scattering

Magnetic scattering experiments were performed in normal-incidence transmission geometry on a magnetic

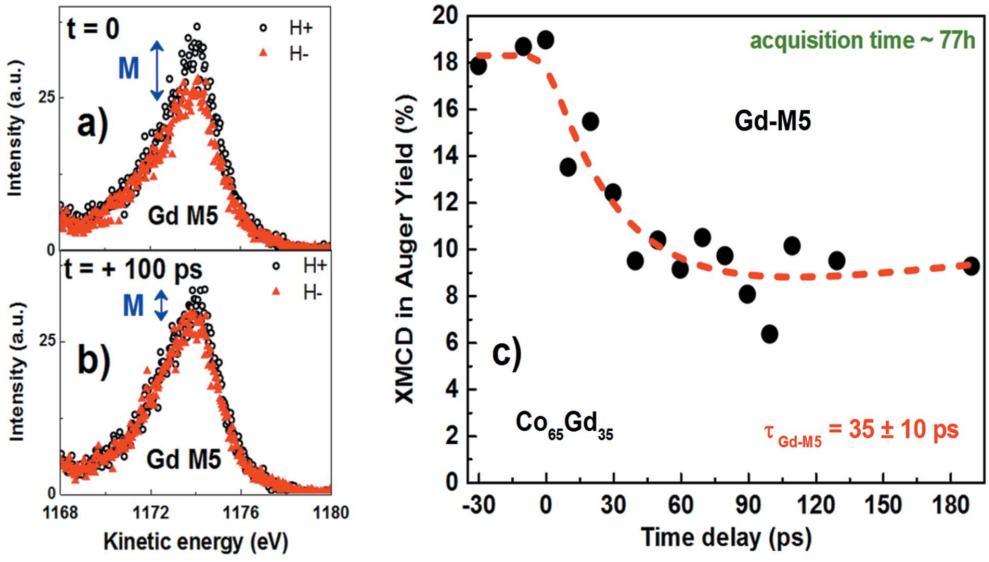

Figure 9
(*a*) Gd-M_5 Auger resonance excited at 1186 eV measured in remanence with two opposite magnetization directions in $Co_{0.65}Gd_{0.35}$ as observed before (*a*) and after (*b*) the laser excitation. (*c*) Time-dependent XMCD signal measured at the Gd-M_5 Auger resonance (black dots). The laser excitation is produced by the 50 fs laser at 800 nm. The red dashed line reproduces the demagnetization dynamics simulated by combining an exponential decay function and an exponential recovery function with time constants of 35 ps and 850 ps, respectively.

(Co 40.4 nm, Pd 0.2 nm) × 20 multilayer, which exhibits out-of-plane anisotropy. This multilayer was sputter deposited onto an X-ray transparent Si_3N_4 membrane. A demagnetization procedure with the external magnetic field oriented perpendicular to the film surface was applied to prepare a remanent magnetization state exhibiting the characteristic worm domain structure. Magnetic force microscopy (MFM) (not shown here) verified its presence and characterized the domain width to be about ∼70 nm. In the scattering experiment this magnetic domain structure gives rise to a ring structure, whose diameter characterizes the domain width (confirming the local MFM image). The statistical deviation from this domain size is reflected in the ring width (Eisebitt *et al.*, 2004). Since the difference in magnetization between the domains is the origin of the scattering contrast, the measured magnetic scattering intensity is proportional to the square of the domain's magnetization (Kortright & Kim, 2000).

The demagnetization induced by an intense short laser pulse takes place on a sub-picosecond time scale (Beaurepaire *et al.*, 1996), which is at least an order of magnitude faster than the expected length of the X-ray probe pulse. Therefore, the demagnetization curve presented in Fig. 10 is a direct measurement of the achieved overall time resolution of the experiment. We used the $\alpha/25$ mode of SOLEIL with a nominal X-ray pulse length of 13 ps FWHM. We remark that the incident photon flux had to be attenuated to avoid saturating the delay line readout electronics. The excellent time resolution of the detection system allows the measurements of all the 200 or 300 consecutive X-ray pulses of the hybrid mode (Fig. 6). Note that all subsequent X-ray pulses, separated by 2.8 ns one from the other, can be used to follow the long-term evolution of the film's magnetization following the femtosecond laser pulse excitation.

The normalized magnetic scattering intensity (pumped/unpumped) is measured as a function of the pump–probe delays at the Co L_3-edge (778 eV). Scattering data are collected using one of the synchrotron bunches in the 200 or 300 bunch sequence (see Fig. 1). The observed magnetization dynamic is shown in Fig. 10 (black dots). The data can be reproduced with the classical demagnetization behaviour (Beaurepaire *et al.*, 1996), which is convoluted with a Gaussian function of 13 ps FWHM representing the achieved overall

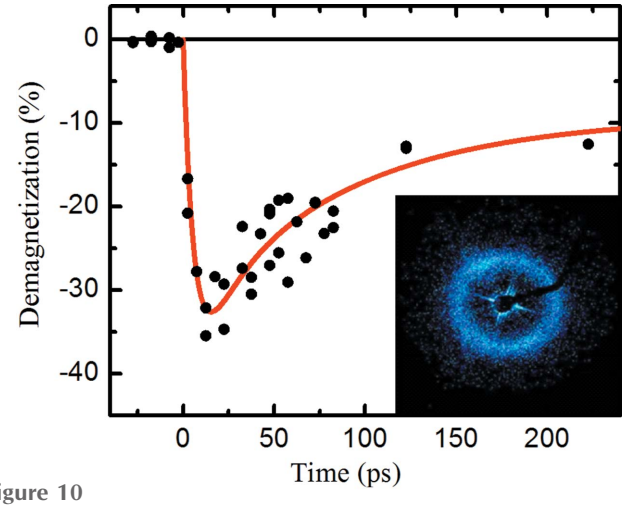

Figure 10
Inset: intensity of the magnetic scattering pattern collected by the 2D+t detector showing the ring-shaped resonant magnetic scattering contribution from the worm-like domains in the CoPd multilayer. Note that this pattern has been accumulated by selecting uniquely the photons emitted by the electron bunch following the laser excitation (see Fig. 1) and normalized to the intensity recorded for revolutions preceding the laser excitation. The intensity integrated over the ring is plotted as a function of the IR pump/X-ray probe delay, thus characterizing the magnetization dynamics at the Co L_3-edge (778 eV) following the laser excitation.

time resolution. The value of about 13 ps thus confirms the expected length of the X-ray pulses and underlines the fact that the achieved time resolution is primarily limited by the X-ray pulse length.

9. Conclusions

The third-generation synchrotron radiation source SOLEIL dedicates one week each semester to low momentum compaction factor (low-α) operation. A specific machine filling is used for user experiments: a sequence of 200 or 300 bunches separated by 2.8 ns occupies half or three-quarters of the synchrotron while an isolated bunch is injected at the centre of the remaining orbit. By reducing the charge per bunch to 95 µA [10 µA] in the sequence and to 65 µA [15 µA] in the isolated bunch, 11 ps [7 ps] FWHM pulse duration is obtained in α/25 [α/100] operation. We have presented examples of experiments performed using soft X-rays at the TEMPO beamline, coupling low-α operation with a high-repetition-rate (up to 282 kHz) femtosecond laser system. We have described the characteristics of the relevant beamline, laser and synchronization systems as well as the specific detection system used for two-dimensional electron and photon detections.

Despite the small bunch charge that is imposed by the desired time resolution, the 200 or 300 bunch sequence results in a total synchrotron current of 19 mA which is high enough to easily align synchrotron and laser beams and to perform efficient sample characterization during the experiments. Thanks to the high laser repetition rate (282 kHz or 141 kHz), photoemission pump–probe experiments can be performed with a good energy resolution and acceptable statistics to follow few meV energy shifts stemming from the laser-induced photovoltage effect.

Surface-sensitive XMCD experiments in Auger detection mode can be performed at transition-metal L_3 and rare-earth M_5 absorption edges. We show that it is possible to investigate magnetization dynamics with chemical resolution and surface sensitivity. The enhanced time resolution of α/25 operation can be applied to rare-earth elements in alloys where the concentrations are larger than 30%. X-ray magnetic scattering experiments have been performed in α/25 operating conditions confirming the expected time resolution of 13 ps as set by the X-ray pulse length. Due to the high efficiency of the applied photon-counting technique, it is possible to perform such experiments even with lower X-ray intensities as in α/100 operation and lower repetition rates as associated with femtoslicing experiments. The expected time resolution of 13 ps has been measured in a resonant scattering pump–probe experiment.

The installation is characterized by a selectable repetition rate for the IR laser excitation and can be adapted to the physical properties of the system of interest.

Acknowledgements

The SOLEIL accelerator physics group acknowledges the diagnostics group and M. Labat in particular for comprehensive electron bunch length measurement campaigns. The authors are grateful for the financial support received as detailed below.

Funding information

Funding for this research was provided by: French National Research Agency via the Labex NIE (award No. ANR-11-LABX-0058-NIE); ERASMUS Mundus exchange program for support of BT; Ile-de-France for DYNAVO Post Doc contract of MT; National Research Agency with project EQUIPEX UNION (award No. ANR-10-EQPX-52).

References

Abo-Bakr, M., Feikes, J., Holldack, K., Kuske, P., Peatman, W. B., Schade, U., Wüstefeld, G. & Hübers, H.-W. (2003). *Phys. Rev. Lett.* **90**, 094801.

Allaria, E., Appio, R., Badano, L., Barletta, W. A., Bassanese, S., Biedron, S. G., Borga, A., Busetto, E., Castronovo, D., Cinquegrana, P., Cleva, S., Cocco, D., Cornacchia, M., Craievich, P., Cudin, I., D'Auria, G., Dal Forno, M., Danailov, M. B., De Monte, R., De Ninno, G., Delgiusto, P., Demidovich, A., Di Mitri, S., Diviacco, B., Fabris, A., Fabris, R., Fawley, W., Ferianis, M., Ferrari, E., Ferry, S., Froehlich, L., Furlan, P., Gaio, G., Gelmetti, F., Giannessi, L., Giannini, M., Gobessi, R., Ivanov, R., Karantzoulis, E., Lonza, M., Lutman, A., Mahieu, B., Milloch, M., Milton, S. V., Musardo, M., Nikolov, I., Noe, S., Parmigiani, F., Penco, G., Petronio, M., Pivetta, L., Predonzani, M., Rossi, F., Rumiz, L., Salom, A., Scafuri, C., Serpico, C., Sigalotti, P., Spampinati, S., Spezzani, C., Svandrlik, M., Svetina, C., Tazzari, S., Trovo, M., Umer, R., Vascotto, A., Veronese, M., Visintini, R., Zaccaria, M., Zangrando, D. & Zangrando, M. (2012). *Nat. Photon.* **6**, 699–704.

Ayvazyan, V., Baboi, N., Bähr, J., Balandin, V., Beutner, B., Brandt, A., Bohnet, I., Bolzmann, A., Brinkmann, R., Brovko, O. I., Carneiro, J. P., Casalbuoni, S., Castellano, M., Castro, P., Catani, L., Chiadroni, E., Choroba, S., Cianchi, A., Delsim-Hashemi, H., Di Pirro, G., Dohlus, M., Düsterer, S., Edwards, H. T., Faatz, B., Fateev, A. A., Feldhaus, J., Flöttmann, K., Frisch, J., Fröhlich, L., Garvey, T., Gensch, U., Golubeva, N., Grabosch, H.-J., Grigoryan, B., Grimm, O., Hahn, U., Han, J. H., Hartrott, M. V., Honkavaara, K., Hüning, M., Ischebeck, R., Jaeschke, E., Jablonka, M., Kammering, R., Katalev, V., Keitel, B., Khodyachykh, S., Kim, Y., Kocharyan, V., Körfer, M., Kollewe, M., Kostin, D., Krämer, D., Krassilnikov, M., Kube, G., Lilje, L., Limberg, T., Lipka, D., Löhl, F., Luong, M., Magne, C., Menzel, J., Michelato, P., Miltchev, V., Minty, M., Möller, W. D., Monaco, L., Müller, W., Nagl, M., Napoly, O., Nicolosi, P., Nölle, D., Nuñez, T., Oppelt, A., Pagani, C., Paparella, R., Petersen, B., Petrosyan, B., Pflüger, J., Piot, P., Plönjes, E., Poletto, L., Proch, D., Pugachov, D., Rehlich, K., Richter, D., Riemann, S., Ross, M., Rossbach, J., Sachwitz, M., Saldin, E. L., Sandner, W., Schlarb, H., Schmidt, B., Schmitz, M., Schmüser, P., Schneider, J. R., Schneidmiller, E. A., Schreiber, H.-J., Schreiber, S., Shabunov, A. V., Sertore, D., Setzer, S., Simrock, S., Sombrowski, E., Staykov, L., Steffen, B., Stephan, F., Stulle, F., Sytchev, K. P., Thom, H., Tiedtke, K., Tischer, M., Treusch, R., Trines, D., Tsakov, I., Vardanyan, A., Wanzenberg, R., Weiland, T., Weise, H., Wendt, M., Will, I., Winter, A., Wittenburg, K., Yurkov, M. V., Zagorodnov, I., Zambolin, P. & Zapfe, K. (2006). *Eur. Phys. J. D*, **37**, 297–303.

Bargheer, M., Zhavoronkov, N., Gritsai, Y., Woo, J. C., Kim, D. S., Woerner, M. & Elsaesser, T. (2004). *Science*, **306**, 1771–1773.

Beaurepaire, E. J. C., Merle, A., Daunois, A. & Bigot, J. Y. (1996). *Phys. Rev. Lett.* **76**, 4250–4253.
Bergeard, N., López-Flores, V., Halté, V., Hehn, M., Stamm, C., Pontius, N., Beaurepaire, E. & Boeglin, C. (2014). *Nat. Commun.* **5**, 3466.
Bergeard, N., Silly, M. G., Krizmancic, D., Chauvet, C., Guzzo, M., Ricaud, J. P., Izquierdo, M., Stebel, L., Pittana, P., Sergo, R., Cautero, G., Dufour, G., Rochet, F. & Sirotti, F. (2011). *J. Synchrotron Rad.* **18**, 245–250.
Boeglin, C., Beaurepaire, E., Halté, V., López-Flores, V., Stamm, C., Pontius, N., Dürr, H. A. & Bigot, J.-Y. (2010). *Nature*, **465**, 458–461.
Bonfim, M., Ghiringhelli, G., Montaigne, F., Pizzini, S., Brookes, N. B., Petroff, F., Vogel, J., Camarero, J. & Fontaine, A. (2001). *Phys. Rev. Lett.* **86**, 3646–3649.
Bonn, M., Funk, S., Hess, C., Denzler, D. N., Stampfl, C., Scheffler, M., Wolf, M. & Ertl, G. (1999). *Science*, **285**, 1042–1045.
Buss, J., Wang, H., Xu, Y., Stoll, S., Zeng, L., Ulonska, S., Denlinger, J., Hussain, Z., Jozwiak, C., Lanzara, A. & Kaindl, R. (2016). APS March Meeting 2016. Abstract C46.00005.(http://meetings.aps.org/link/BAPS.2016.MAR.C46.5).
Cautero, G., Sergo, R., Stebel, L., Lacovig, P., Pittana, P., Predonzani, M. & Carrato, S. (2008). *Nucl. Instrum. Methods Phys. Res. A*, **595**, 447–459.
Couprie, M. E. & Filhol, J. M. (2008). *C. R. Phys.* **9**, 487–506.
Eisebitt, S., Lüning, J., Schlotter, W. F., Lörgen, M., Hellwig, O., Eberhardt, W. & Stöhr, J. (2004). *Nature (London)*, **432**, 885–888.
Eschenlohr, A., Sultan, M., Melnikov, A., Bergeard, N., Wieczorek, J., Kachel, T., Stamm, C. & Bovensiepen, U. (2014). *Phys. Rev. B*, **89**, 214423.
Faatz, B., Baboi, N., Ayvazyan, V., Balandin, V., Decking, W., Duesterer, S., Eckoldt, H.-J., Feldhaus, J., Golubeva, N., Honkavaara, K., Koerfer, M., Laarmann, T., Leuschner, A., Lilje, L., Limberg, T., Noelle, D., Obier, F., Petrov, A., Ploenjes, E., Rehlich, K., Schlarb, H., Schmidt, B., Schmitz, M., Schreiber, S., Schulte-Schrepping, H., Spengler, J., Staack, M., Tavella, F., Tiedtke, K., Tischer, M., Treusch, R., Vogt, M., Willner, A., Bahrdt, J., Follath, R., Gensch, M., Holldack, K., Meseck, A., Mitzner, R., Drescher, M., Miltchev, M., Rönsch-Schulenburg J. & Rossbach, J. (2011). *Nucl. Instrum. Methods Phys. Res. A*, **635**, S2–S5.
Fan, T., Grychtol, P., Knut, R., Hernández-García, C., Hickstein, D. D., Zusin, D., Gentry, C., Dollar, F. J., Mancuso, C. A., Hogle, C. W., Kfir, O., Legut, D., Carva, K., Ellis, J. L., Dorney, K. M., Chen, C., Shpyrko, O. G., Fullerton, E. E., Cohen, O., Oppeneer, P. M., Milosevic, D. B., Becker, A., Jaron-Becker, A. A., Popmintchev, T., Murnane, M. M. & Kapteyn, H. C. (2015). *Proc. Natl Acad. Sci.* **112**, 14206–14211.
Frietsch, B., Bowlan, J., Carley, R., Teichmann, M., Wienholdt, S., Hinzke, D., Nowak, U., Carva, K., Oppeneer, P. M. & Weinelt, M. (2015). *Nat. Commun.* **6**, 8262.
Funk, T., Deb, A., George, S. J., Wang, H. & Cramer, S. P. (2005). *Coord. Chem. Rev.* **249**, 3–30.
Higley, D. J., Hirsch, K., Dakovski, G. L., Jal, E., Yuan, E., Liu, T., Lutman, A. A., MacArthur, J. P., Arenholz, E., Chen, Z., Coslovich, G., Denes, P., Granitzka, P. W., Hart, P., Hoffmann, M. C., Joseph, J., Le Guyader, L., Mitra, A., Moeller, S., Ohldag, H., Seaberg, M., Shafer, P., Stöhr, J., Tsukamoto, A., Nuhn, H. D., Reid, A. H., Dürr, H. A. & Schlotter, W. F. (2016). *Rev. Sci. Instrum.* **87**, 033110.
Ingold, G., Beaud, P., Johnson, S. L., Grolimund, D., Schlott, V., Schmidt, T. & Streun, A. (2007). *Synchrotron Radiat. News*, **20**, 39–43.
Jankowiak, A. & Wüstefeld, G. (2013). *Synchrotron Radiat. News*, **26**, 22.
Khan, S. K., Holldack, T., Kachel, R., Mitzner, R. & Quast, T. (2006). *Phys. Rev. Lett.* **97**, 074801.
Koopmans, B., Malinowski, G., Dalla Longa, F., Steiauf, D., Fähnle, M., Roth, T., Cinchetti, M. & Aeschlimann, M. (2009). *Nat. Mater.* **9**, 259–265.
Kortright, J. B. & Kim, S.-K. (2000). *Phys. Rev. B*, **62**, 12216–12228.
Kozina, M., Hu, T., Wittenberg, J. S., Szilagyi, E., Trigo, M., Miller, T. A., Uher, C., Damodaran, A., Martin, L., Mehta, A., Corbett, J., Safranek, J., Reis, D. A. & Lindenberg, A. M. (2014). *Struct. Dyn.* **1**, 034301.
Long, J. P., Sadeghi, H. R., Rife, J. C. & Kabler, M. N. (1990). *Phys. Rev. Lett.* **64**, 1158–1161.
López-Flores, V., Arabski, J., Stamm, C., Halté, V., Pontius, N., Beaurepaire, E. & Boeglin, C. (2012). *Phys. Rev. B*, **86**, 014424.
López-Flores, V., Bergeard, N., Halté, V., Stamm, C., Pontius, N., Hehn, M., Otero, E., Beaurepaire, E. & Boeglin, C. (2013). *Phys. Rev. B*, **87**, 214412.
Marsi, M., Belkhou, R., Grupp, C., Panaccione, G., Taleb-Ibrahimi, A., Nahon, L., Garzella, D., Nutarelli, D., Renault, E., Roux, R., Couprie, M. E. & Billardon, M. (2000). *Phys. Rev. B*, **61**, R5070–R5073.
Marsi, M., Couprie, M. E., Nahon, L., Garzella, D., Hara, T., Bakker, R., Billardon, M., Delboulbé, A., Indlekofer, G. & Taleb-Ibrahimi, A. (1997). *Appl. Phys. Lett.* **70**, 895–897.
Ogawa, M., Yamamoto, S., Fujikawa, K., Hobara, R., Yukawa, R., Yamamoto, S., Kitagawa, S., Pierucci, D., Silly, M. G., Lin, C.-H., Liu, R.-Y., Daimon, H., Sirotti, F., Tang, S.-J. & Matsuda, I. (2013). *Phys. Rev. B*, **88**, 165313.
Ojeda, J., Arrell, C. A., Grilj, J., Frassetto, F., Mewes, L., Zhang, H., van Mourik, F., Poletto, L. & Chergui, M. (2016). *Struct. Dyn.* **3**, 023602.
Pfeifer, T., Spielmann, C. & Gerber, G. (2006). *Rep. Prog. Phys.* **69**, 443–505.
Polack, F., Silly, M., Chauvet, C., Lagarde, B., Bergeard, N., Izquierdo, M., Chubar, O., Krizmancic, D., Ribbens, M., Duval, J.-P., Basset, C., Kubsky, S. & Sirotti, F. (2010). *AIP Conf. Proc.* **1234**, 185–188.
Prigent, P., Hollander, Ph., Labat, M., Couprie, M. E., Marlats, J. L., Laulhé, C., Luning, J., Moreno, T., Morin, P. & Nadji, A. (2013). *J. Phys. Conf. Ser.* **425**, 072022.
Radu, I., Vahaplar, K., Stamm, C., Kachel, T., Pontius, N., Dürr, H. A., Ostler, T. A., Barker, J., Evans, R. F. L., Chantrell, R. W., Tsukamoto, A., Itoh, A., Kirilyuk, A., Rasing, Th. & Kimel, A. V. (2011). *Nature (London)*, **472**, 205–208.
Rettig, L., Dornes, C., Thielemann-Kühn, N., Pontius, N., Zabel, H., Schlagel, D. L., Lograsso, T. A., Chollet, M., Robert, A., Sikorski, M., Song, S., Glownia, J. M., Schüssler-Langeheine, C., Johnson, S. L. & Staub, U. (2016). *Phys. Rev. Lett.* **116**, 257202.
Ricaud, J. P., Betinelli-Deck, P., Bisou, J., Elattaoui, X., Laulhé, C., Monteiro, P., Nadolski, L. S., Ravy, S., Renaud, G., Silly, M. G. & Sirotti, F. (2011). *13th International Conference on Accelerator and Large Experimental Physics Control Systems (ICALEPCS2011)*, 10–14 October 2011, Grenoble, France. WEPMS026.
Sacchi, M., Jaouen, N., Popescu, H., Gaudemer, R., Tonnerre, J. M., Chiuzbaian, S. G., Hague, C. F., Delmotte, A., Dubuisson, J. M., Cauchon, G., Lagarde, B. & Polack, F. (2013). *J. Phys. Conf. Ser.* **425**, 072018.
Schönlein, R. W., Chattopadhyay, S., Chong, H. H., Glover, T. E., Heimann, P. A., Shank, C. V., Zholents, A. A. & Zolotorev, M. S. (2000). *Science*, **287**, 2237–2340.
Silva, F., Teichmann, S. M., Cousin, S. L., Hemmer, M. & Biegert, J. (2015). *Nat. Commun.* **6**, 6611.
Sirotti, F., Girlando, S., Prieto, P., Floreano, L., Panaccione, G. & Rossi, G. (2000). *Phys. Rev. B*, **61**, R9221–R9224.
Spencer, B. F., Graham, D. M., Hardman, S. J. O., Seddon, E. A., Cliffe, M. J., Syres, K. L., Thomas, A. G., Stubbs, S. K., Sirotti, F., Silly, M. G., Kirkham, P. F., Kumarasinghe, A. R., Hirst, G. J., Moss, A. J., Hill, S. F., Shaw, D. A., Chattopadhyay, S. & Flavell, W. R. (2013). *Phys. Rev. B*, **88**, 195301.
Stamm, C., Kachel, T., Pontius, N., Mitzner, R., Quast, T., Holldack, K., Khan, S., Lupulescu, C., Aziz, E. F., Wietstruk, M., Dürr, H. A. & Eberhardt, W. (2007). *Nat. Mater.* **6**, 740–743.
Teichmann, S. M., Silva, F., Cousin, S. L., Hemmer, M. & Biegert, J. (2016). *Nat. Commun.* **7**, 11493.

Tordeux, M. A., Barros, J., Bence, A., Brunelle, P., Hubert, N., Labat, M., Lebasque, P., Nadji, A., Nadolski, L. S., Pollina, J.-P. & Evain, C. (2012). *Proceedings of the 2012 International Particle Accelerator Conference (IPAC12)*, 20–25 May 2012, New Orleans, USA, pp. 1608–1610.
Vicentin, F. C., Turchini, S., Yubero, F., Vogel, J. & Sacchi, M. (1995). *J. Electron Spectrosc. Relat. Phenom.* **74**, 187–194.
Wang, H., Xu, Y., Ulonska, S., Robinson, J. S., Ranitovic, P. & Kaindl, R. A. (2015). *Nat. Commun.* **6**, 7459.
Widdra, W., Bröcker, D., Giessel, T., Hertel, I. V., Krüger, W., Liero, A., Noack, F., Petrov, V., Pop, D., Schmidt, P. M., Weber, R., Will, I. & Winter, B. (2003). *Surf. Sci.* **543**, 87–94.
Wietstruk, M., Melnikov, A., Stamm, C., Kachel, T., Pontius, N., Sultan, M., Gahl, C., Weinelt, M., Dürr, H. A. & Bovensiepen, U. (2011). *Phys. Rev. Lett.* **106**, 127401.
Yabashi, M., Tanaka, H. & Ishikawa, T. (2015). *J. Synchrotron Rad.* **22**, 477–484.